ADVANCED ENERGY MATERIALS
www.advenergymat.de

Direct In Situ Determination of the Surface Area and Structure of Deposited Metallic Lithium within Lithium Metal Batteries Using Ultra Small and Small Angle Neutron Scattering

*Christophe Didier, Elliot P. Gilbert, Jitendra Mata, and Vanessa K. Peterson**

Despite being the major cause of safety and performance issues in lithium metal batteries, experimental difficulties in quantifying directly the morphology of lithium deposited at electrode surfaces have meant that the mechanism of metallic lithium growth within batteries remains elusive. This study demonstrates that quantitative detail about the morphology of metallic lithium within batteries can be derived non-destructively and directly using in situ ultra-small and small-angle neutron scattering. This information is obtained over a large electrode area in cells where lithium deposition processes are typical of real-world applications. Complex variations of surface area and interfacial distances 1–10 µm and 100–300 nm are revealed in size that are influenced by current density and cell cycling history, providing valuable insight into the growth of metallic lithium features detrimental to battery performance. Such quantitative insight into the process of lithium growth is required for the development of safer high-performance lithium metal batteries.

1. Introduction

Considerable effort to improve lithium-ion batteries (LIBs) over the past 30 years[1] has enabled the use of portable electronics and electric vehicles. There is interest to replace commonly used LIB electrodes such as graphite with lithium metal because of its order-of-magnitude larger specific capacity; however, rechargeable lithium metal batteries (LMBs) are plagued by low efficiency and rapid capacity fade.[2] These LMB performance issues are attributed primarily to the formation of high surface area microstructures at the lithium surface, with these creating short-circuits between electrodes and irreversibly separating from the electrode after partial dissolution resulting in electrochemically inactive "dead lithium".[2a,3] Preventing and understanding the formation of lithium structures detrimental to LMB performance has been the aim of recent and intensive research,[4] the success of which is underpinned by quantitative methods that can reliably probe such lithium microstructures. The experimental difficulty in observing deposited lithium has meant that the mechanism of lithium deposition and microstructure development in LMBs is still poorly understood.

Electron and optical microscopy studies have revealed the morphology of deposited lithium with some success, with commonly reported structures in liquid electrolyte LMBs being so-called whiskers, mosses, and dendrites, while noting a lack of naming convention.[4a,5] Whiskers are reported to appear as needles ≈ 100 nm wide and up to 10 µm long (Figure S1A, Supporting Information). The description of mossy lithium is given to a porous layer up to several hundreds of microns thick, comprising interconnected objects of diameter 0.1 to 10 µm (Figure S1B, Supporting Information). Mossy lithium is reported to arise from the interweaving and broadening of whiskers,[5b,c,6] although it is unclear if all whiskers become mossy. Dendrites are reported as 100–500 µm long fractal filaments ≈ 1 µm thick, sometimes forming dense bushes.[5d] Historically, deposited lithium has been examined *post mortem* after extraction from the LMB – a mechanical process that potentially changes the electrode surface. In situ techniques that examine lithium within the LMB have enabled remarkable progress in understanding the parameters that influence lithium growth, notably including optical and electron microscopy,[2b,5a–d,6,7] however, such methods are limited to examining a small sample area within model cells that likely do not accurately represent the typical LMB chemical environment.[8] In situ nuclear mangetic resonance (NMR) spectroscopy has enabled quantitative time-resolved macroscopic determination of the amount of surface

C. Didier, E. P. Gilbert, J. Mata, V. K. Peterson
Australian Centre for Neutron Scattering
Australian Nuclear Science and Technology Organisation
Locked Bag 2001, Kirrawee DC, NSW 2232, Australia
E-mail: vanessa.peterson@ansto.gov.au
J. Mata
School of Chemistry
University of New South Wales
Sydney, NSW 2052, Australia

The ORCID identification number(s) for the author(s) of this article can be found under https://doi.org/10.1002/aenm.202301266

DOI: 10.1002/aenm.202301266

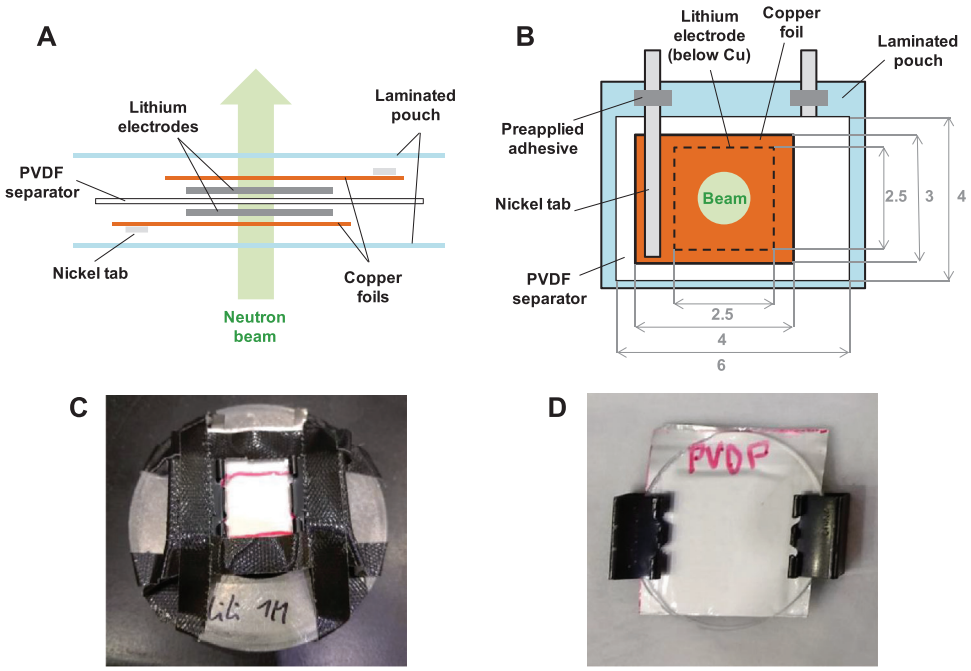

Figure 1. In situ cell construction. A) Side view schematic of the lithium pouch cell. B) Front view schematic of the lithium pouch cell. Top laminated pouch omitted for clarity and distances in cm. The 1.2 cm diameter neutron beam corresponds to that used in the USANS experiment. C) Photograph of the in situ cell between quartz plates held by clips (behind tape) mounted on a metallic holder. D) Photograph of the electrolyte-wet PVDF sealed in a laminated pouch between quartz plates held by clips. PVDF = polyvinylidene difluoride.

deposited lithium, but the size information concerning microstructure is limited, and the technique also requires small model cells that may not be representative of processes within larger LMBs.[9]

Small- and ultra-small-angle neutron scattering (SANS and USANS, respectively,) can be used to study the morphology of structures within objects on length scales typically 1 nm to 10 µm and within the range reported for deposited lithium structures. These techniques are sensitive to neutron scattering length density (SLD) inhomogeneities in a sample, with the scattered intensity proportional to the inhomogeneity quantity and surrounding contrast given by the square of the difference of the SLD. SLD inhomogeneities arise from elemental and isotopic density variations, as found at the interface between two phases. Scattering intensity variations with scattering vector Q depend on the spatial distribution of such inhomogeneities, which can be related to the size and shape of those objects. There are large advantages to studying LIBs and LMBs using SANS and USANS, where the high penetration of neutrons easily permits full transmission in situ measurements of components within typical electrochemical cells, and where information is averaged over a very large portion of the cell, in contrast to microscopy studies. Despite these advantages, only a limited number of in situ SANS and no USANS studies of batteries have been reported. Relatively good sensitivity of SANS to electrode surface changes has been shown, such as to lithium sulfide deposition within porous carbon,[10] to the formation of the solid electrolyte interphase (SEI) on the surface of lithiated graphite[11] and lithium titanate,[12] and to interfacial changes between lithiated graphite phases.[13] Increased SANS intensity from a symmetrical LMB post-cycling confirmed the sensitivity of SANS to changes at a lithium electrode, although morphological details were not derived,[13b] and SANS profile changes from an LMB on cycling revealed the formation of lithium features 1–10 nm, although a quantitative description of the scattering from lithium was not able to be made.[14]

Here, we build on these previous concepts to demonstrate that in situ SANS and USANS can provide a quantitative description of the morphology and growth process of metallic lithium deposited within a symmetrical LMB containing liquid electrolyte. We first characterize the signal from individual components to guide the construction of the LMB and our understanding of the scattered intensity, which we subsequently evaluate using simple models to quantitatively describe the in situ SANS and USANS data. Using this approach, we derive for the first time parameters such as the surface area and particle size of deposited lithium structures after applied galvanostatic cycling, over an electrode area that has lithium deposition processes representative of the whole cell.

2. Results

A flat laminated pouch cell with a relatively simple and flexible assembly (**Figure 1**), similar to that used in other work,[13] was chosen. Component selection and contribution to scattering are discussed in Note S1 (Supporting Information) with Figures S2–S8 and Tables S1 and S2 (Supporting Information). Several cells were made, one underwent two "charge" and "discharge" cycles at a current density of 20 mA cm^{-2}, while the other underwent four consecutive "charge" followed by four consecutive "discharge" processes at 2 mA cm^{-2}, followed by one further "discharge" at

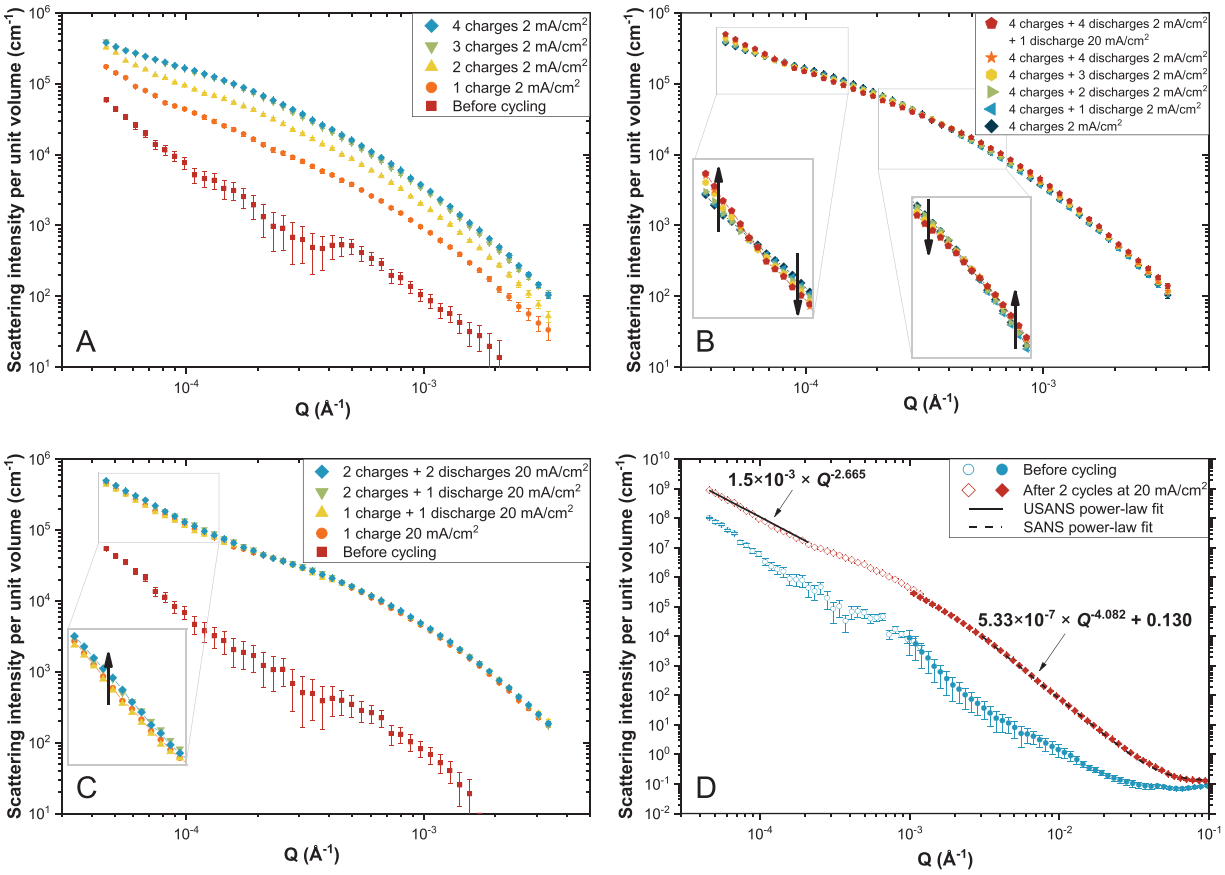

Figure 2. Scattering data from the in situ cell before and after electrochemical processes. A) B) C) Slit-smeared USANS scattering shown as the differential cross-section per unit volume of lithium after subtraction of scattering from electrochemically inactive components from an in situ cell A) before cycling and after one, two, three, and four consecutive "charges" at 2 mA cm^{-2}, and B) after four "charges" and followed by one, two, three, and four consecutive "discharges" at 2 mA cm^{-2}, and an additional "discharge" at 20 mA cm^{-2}. C) From an in situ cell before cycling and after alternating "charges" and "discharges" at 20 mA cm^{-2}. Arrows are visual guides emphasizing intensity change. Corresponding raw data before subtraction for A), B), and C) are shown in Figure S8A–C (Supporting Information), respectively. D) Desmeared USANS (open symbols) and SANS (closed symbols) scattering shown as a differential cross-section per unit volume for lithium in the cell before (blue circles) and after (red diamonds) two cycles at 20 mA cm^{-2}. Power-law exponents for lithium in the cell after two cycles were extracted by fitting $A \times Q^{-n}$ to smeared USANS data and $A \times Q^{-n} + B$ to SANS data, between $4 \times 10^{-5} < Q < 2 \times 10^{-4}$ Å^{-1} and $3 \times 10^{-3} < Q < 10^{-1}$ Å^{-1}, respectively. Refined values were $A = 1.5(2) \times 10^{-3}$ and $n = 2.665(16)$ for USANS, and $A = 5.33(18) \times 10^{-7}$, $B = 0.130(4)$, and $n = 4.082(7)$ for SANS. Corresponding data before desmearing for D) are shown in Figure S9A (Supporting Information).

20 mA cm^{-2}. Each galvanostatic step was applied for 1 h and the circuit was left open for 3–5 h during which USANS data were measured. SANS data of the 20 mA cm^{-2} battery were measured prior to and following cycling in the USANS experiment.

USANS data measured between each galvanostatic step for the cell cycled at 2 mA cm^{-2} are shown in **Figure 2**A for the first four charges and Figure 2B for the following four 2 mA cm^{-2} discharges and the discharge at 20 mA cm^{-2}. USANS data of the cell charged and discharged twice at 20 mA cm^{-2} are shown in Figure 2C. Overall scattered intensity from the cell charged at 2 mA cm^{-2} increased gradually during the first three charges with only minor variation post maximum, including after discharge at 20 mA cm^{-2}. At 20 mA cm^{-2}, the maximum scattering intensity is reached after the first cycle, with little variation thereafter. Both cells have a similar maximum scattering intensity, reaching an order of magnitude greater than before cycling; the initial intensity is never recovered, confirming the irreversibility of lithium surface transformations. Overall USANS data of the cell after galvanostatic cycling follows similar trends with an initial power-law decrease in intensity at $Q < 10^{-4}$ Å^{-1} that becomes a gentler slope at intermediate Q and a steeper slope at $Q > 10^{-3}$ Å^{-1}.

USANS and SANS data for lithium in the cell before and after 2 cycles at 20 mA cm^{-2} are shown in Figure 2D. Subtraction of inactive components does not substantially change the scattering after cycling (Figure S5B, Supporting Information) as a result of the order of magnitude increase of scattering from lithium, this being a larger increase than previously reported using in situ SANS for lithium metal cells,[13b,14] possibly as a result of the relatively higher current density. The transmission of neutrons through the cell in the USANS region decreased substantially after cycling (Table S1, Supporting Information) as a result of this increased coherent scattering, while attenuation from absorption and incoherent processes remained constant, as expected. Transmission after attenuation from coherent scattering (T_{SAS} = 53%)

suggests the potential for some multiple scattering contamination that may slightly decrease intensity at lower Q, noting a relatively small effect is expected for samples with $T_{SAS} \approx 50\%$ measured on the same instrument.[15]

Since lithium metal being the only electrochemically active material in the cell, the coherent scattering increase is assumed to originate from the lithium surface. Data contain information from both electrodes, even though the lithium surface on each side of the cell may differ following reversible lithium deposition. Data show a distinct change in shape before and after cycling (Figure 2D), with post-cycling data exhibiting two approximately power-law decreases separated by a broad shoulder in the intermediate Q range, having $Q^{-2.665(16)}$ slope in the USANS region from $Q = 4 \times 10^{-5}$ to 2×10^{-4} Å^{-1} and $Q^{-4.082(7)}$ slope in the SANS region from $Q = 3 \times 10^{-3}$ to 10^{-1} Å^{-1}. The Q^{-4} variation at low Q is consistent with smooth interfacial scattering and increased surface area post-cycling, as observed using other techniques.[16] Scattering from the bulk foil volume that dominates pre-cycling is negligible post-cycling.

3. Discussion

3.1. Surface Area from Porod's Law

In non-particulate, non-uniform systems, scattering can originate from interfaces between volumes of different SLD, known as phases,[17] and we therefore, postulate that scattering from the cell post-cycling originates from the lithium–electrolyte interface, with lithium metal and electrolyte taken as separate homogeneous volumes. A sharp change of SLD around "smooth" boundaries at the nanoscale between phases results in the differential scattering cross-section per unit volume ($\frac{d\Sigma}{d\Omega}$) following Porod's law at sufficiently high Q:[17]

$$\frac{d\Sigma}{d\Omega} = P \times Q^{-4} + B \tag{1}$$

with B accounting for the background and the Porod exponent P the contribution from all surfaces:

$$P = 2\pi \sum_i \left[\left(\Delta\rho_i\right)^2 \times \frac{S_i}{V} \right] \tag{2}$$

where S_i is the surface area at interface i between two phases, $\Delta\rho_i$ is the SLD contrast between the phases either side of the interface, and V is the volume occupied by the phases. The model can be extended to any number of phases, and development considering two or three phases for lithium in the cell is given in Note S2 (Supporting Information).

The increase of scattering in the cell post-cycling is consistent with increased surface area.[16] The Q^{-4} slope from the cell post-cycling is sustained at $Q > 2 \times 10^{-3}$ Å^{-1} ($Q^{-1} < 50$ nm), suggesting the absence of particles or porosity < 50 nm, noting that features < 100 nm are rarely observed for deposited lithium, despite complex micrometer scale morphology shown for deposited lithium by optical and scanning electron microscopy.[4a,5] A Porod's law description of the differential scattering cross-section per unit volume of the cell after two cycles at 20 mA cm^{-2} in the SANS range $2 \times 10^{-3} < Q < 10^{-1}$ Å^{-1} (Figure S9B, Supporting Information) yields P = 78.0(3) × 10^{-8} Å^{-4}.cm^{-1} and B = 0.118(4) cm^{-1}, corresponding to a surface area per unit volume S_V = 19.08(7) × 10^3 cm^2 cm^{-3} in the two-phase system and S_V = 35.57(14) × 10^3 cm^2 cm^{-3} in the three-phase system.

The surface area determined from Porod's law is compared to quantitative measurements of surface area reported using in situ X-ray tomography[7a,18] and *post mortem* gas adsorption using Brunauer–Emmett–Teller (BET) theory[16] in **Table 1**. Quantitative reports of the surface area of cycled lithium are scarce, with qualitative descriptions from microscopy measurements substantially more common. We note inconsistency in reported surface areas per unit volume for lithium determined with X-ray tomography with Sadd et al.[18b] reporting values ≈ 18 × 10^3 cm^2 cm^{-3}, Taiwo et al.[7a] between 0.05 and 0.6 × 10^3 cm^2 cm^{-3}, and Pan et al.[18a] ≈ 0.05 × 10^3 cm^2 cm^{-3}. Only Taiwo et al. report a surface area per unit area that can be used for comparison with our data reported here, while the surface area they determined using in situ X-ray tomography[7a] is smaller than that measured using SANS or gas sorption (Table 1). X-ray tomography severely underestimates lithium surface area because of its ≈ 1 µm resolution limitation. Description of USANS data by the Debye–Anderson–Brumberger (DAB) model (see later section) confirms that micrometric-scale lithium features contribute to surface area.

Only two reports of gas adsorption determined lithium surface area are found,[16] perhaps due to the experimental need to extract foils from the cell, requiring washing and drying under an inert atmosphere, and unconventional use of argon as the adsorbent. A comparison of surface area per unit mass S_M excluding excess lithium is presented in Note S3, Figure S10, and Table S3 (Supporting Information) and substantial differences are observed between SANS and gas adsorption, and between gas adsorption reports. The surface area per unit area S_A obtained from SANS here, less prone to thickness uncertainty (Note S4, Supporting Information), and by Weber et al. using gas adsorption are within an order of magnitude (Table 1). A smaller S_A is reported from gas adsorption than from SANS, likely as a result of the limited probing of internal surface in gas adsorption measurements, seen in Figure S1B (Supporting Information), as evidenced by the increase in surface area measured for pulverized samples.[16b] Insufficient information was given by Saito et al. to enable the determination of surface area per unit area. We note experimental differences likely influencing the surface area of lithium between this work and that of Saito et al. and Weber et al., including differences in cycling protocol, electrolyte, cell construction, as well as the substantial amount of lithium remaining attached to the separator after extraction from the cell in the work of Weber et al. These results highlight the applicability of SANS for the direct and representative determination of the surface area of lithium metal within a cell during cycling, however, further experiments are needed to discriminate between the suitability of two- and three-phase models.

3.2. Surface Area and Whisker Size Obtained from Debye–Anderson–Brumberger Modeling

The slope at $Q < 10^{-4}$ Å^{-1} and shoulder ≈10^{-3} Å^{-1} in the USANS data cannot be modeled by Porod's law and the DAB model

Table 1. Surface area determined from SANS and that reported using X-ray microtomography and gas adsorption. Surface area of deposited lithium calculated from SANS data of the in situ cell after two cycles at 20 mA cm^{-2} (Figure S9B, Supporting Information) using Porod's law for two- and three-phase models, alongside the reported surface area of lithium metal in cells post-cycling obtained using X-ray tomography and gas adsorption with Brunauer–Emmett–Teller (BET) theory. Weber et al. report ex situ data for lithium after 10 cycles extracted from the cell as foil plated on copper or powder scraped from copper, indicated as "foil" and "powder", respectively. Standard uncertainties estimated from least-square regression are shown in parentheses.

	Surface area per unit volume [S_V, 10^3 cm^2 cm^{-3}]	Surface area per unit mass [S_M, 10^3 cm^2 g^{-1}]	Surface area per unit area [S_A, cm^2 cm^{-2}]
SANS Porod model			
2 cycles 20 mA cm^{-2} (2 phase)	19.08(7)	38.56(15)	381.7(1.5)
2 cycles 20 mA cm^{-2} (3 phase)	35.57(14)	71.8(3)	711(3)
Gas adsorption (Weber et al.)			
1 cycle 1.2 and 0.48 mA cm^{-2}	Not reported	30 (foil)	30 (foil)
4 cycles 1.2 and 0.48 mA cm^{-2}		75 (foil)	75 (foil)
10 cycles 1.2 and 0.48 mA cm^{-2}		150 (foil) & 250 (powder)	150 (foil) & 250 (powder)
Gas adsorption (Saito et al.)			
1 h discharge 3 mA cm^{-2}	Not reported	25	Not reported
6 cycles 1 and 0.2 mA cm^{-2}		132	
6 cycles 1 and 3 mA cm^{-2}		258	
X-ray tomography (Taiwo et al.)			
10 cycles	0.05	Not reported	0.175
70 cycles	0.4		5.2
135 cycles	0.6		10.8

was used to describe data in the combined SANS and USANS region.[19] The DAB model considers a non-particulate multiphase system characterized by a correlation length L that is related to the average distance between interfaces, with differential scattering cross-section $\frac{d\Sigma}{d\Omega}$:[19a]

$$\frac{d\Sigma}{d\Omega} = D \times \frac{L^3}{\left[1 + \left(QL\right)^2\right]^2} \tag{3}$$

where D is a scaling factor and D/L is related to the surface area similarly to Porod's constant:[19a]

$$D/L = 2\pi \sum_i \left[\left(\Delta\rho_i\right)^2 \times \frac{S_i}{V}\right] \tag{4}$$

where S_i is the surface area at the interface i between two phases, $\Delta\rho_i$ is the SLD contrast between phases either side of the interface and V is the volume occupied by all phases. Derivation of the surface area for two and three-phase systems follow those for Porod's law.

In this model, scattering at large Q follows Q^{-4}, as consistent with Porod's law, and approaches a soft maximum at $Q = 1/L$, where the shoulder at $\approx 10^{-3}$ $Å^{-1}$ yields a correlation length close to 100 nm. The slope at $Q < 10^{-4}$ $Å^{-1}$ in our data is attributed to scattering from SLD heterogeneities $>1/Q_{min} \approx 2$ µm, where Q_{min} is the smallest experimentally accessible scattering wavevector. This slope can be modeled by a second DAB term with larger L.[19a] To distinguish between the two contributions, the scaling factor and correlation length of lithium features of size < 1 µm and > 1 µm are denoted D_{nano} and L_{nano}, and D_{micro} and L_{micro}, respectively. The complete model used to describe the differential scattering cross-section $\frac{d\Sigma}{d\Omega}$ is therefore given by:

$$\frac{d\Sigma}{d\Omega} = D_{nano} \times \frac{L_{nano}^3}{\left[1 + \left(QL_{nano}\right)^2\right]^2} + D_{micro} \times \frac{L_{micro}^3}{\left[1 + \left(QL_{micro}\right)^2\right]^2} + B \tag{5}$$

with background constant B. Assuming both micrometric and nanometric inhomogeneities arise from lithium-electrolyte interfaces, the surface area is given by the sum:

$$D_{nano}/L_{nano} + D_{micro}/L_{micro} = 2\pi \sum_i \left[\left(\Delta\rho_i\right)^2 \times \frac{S_i}{V}\right] \tag{6}$$

The bimodal DAB model for two different-sized inhomogeneities provides a reasonable description of USANS and SANS data for lithium in the cell post-cycling at 20 mA cm^{-2} (**Figure 3**). Refined model parameters (Table S4, Supporting Information) reflect information from both electrodes, where lithium is alternately deposited on one side and removed from the other in a process involving the partial redissolution of previously deposited lithium. Microscopy confirmed the growth of highly divided surface features on the electrode where deposition occurs, however, dissolution from an initially smooth lithium surface results in the formation of > 10 µm pits that generate large surface area morphologies only after current reversal.[20] As a consequence, SANS measured during the first set of "charges" may be mostly influenced by the electrode where deposition occurs first, whereas on

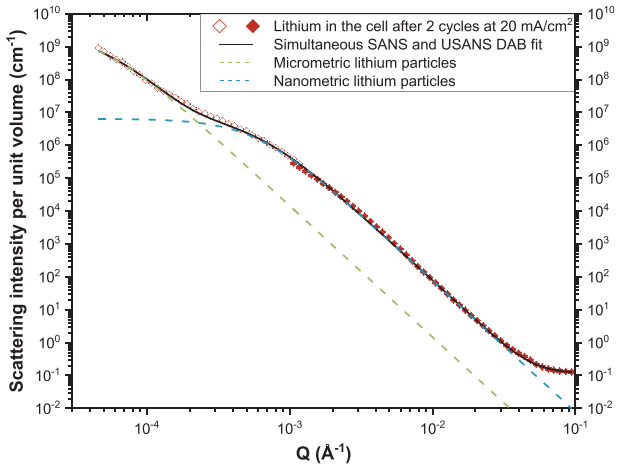

Figure 3. Bimodal DAB modelling of scattering data of the in situ cell. SANS (closed symbols) and desmeared USANS (open symbols) data of lithium in the in situ cell after 2 cycles at 20 mA cm^{-2} and the corresponding DAB model calculation. The model was simultaneously refined against SANS and slit-smeared USANS data, with smearing applied to the model, as shown in Figure S9C (Supporting Information), and refined parameters in Table S4 (Supporting Information).

"discharge" extracted parameters may reflect averaged information from both electrodes.

The sum of D_{nano}/L_{nano} and D_{micro}/L_{micro} is 78.9(7) × 10^{-8} $Å^{-4}$ cm^{-1}, in agreement with the refined Porod parameter P = 78.0(3) × 10^{-8} $Å^{-4}.cm^{-1}$, confirming consistency of the derived surface area between the two methods. D_{nano}/L_{nano} >> D_{micro}/L_{micro}, hence, 98% of surface area arises from nanometric features, with the surface area arising from micrometric features close to $S_V(2) = 0.4 \times 10^3$ cm^2 cm^{-3} (S_A = 8 cm^2 cm^{-2}), comparable to the surface area of surface deposited lithium obtained using in situ X-ray tomography (Table 1) as limited by the micrometric resolution of the technique.[7a,18a] The refined correlation length corresponds to the average distance between lithium/electrolyte interfaces separating statistically homogeneous volumes, which can be related to the size of deposited lithium features and electrolyte-filled pores between them through Babinet's principle.[21] The determined L_{nano} = 169.4(11) nm is similar to the width of so-called whiskers (Figure S1A, Supporting Information) as well as the nanoporosity within mossy layers observed using electron microscopy.[4a,5c,e,22] The determined value of L_{micro} = 2.06(5) µm is similar to the size of microscopic pores within mossy lithium (Figure S1B, Supporting Information) and to the width of dendrites observed using optical and electron microscopies.[4a,5a,c,d] D_{nano} and D_{micro} are quantitatively related to the lithium/electrolyte interface separating statistically homogeneous volumes at distances L_{nano} and L_{micro}, respectively. As lithium volume expansion is not considered, D_{nano} and D_{micro} scale with the areal quantity of surfaces and not the volume concentration of surfaces conventionally expected. The background parameter B may be related to inhomogeneities within the SEI. as explained in Note S2 (Supporting Information), however, this contribution is small in our data limiting further interpretation. A schematic illustration of lithium structures visible in SANS at different length scales is shown in Figure S16 (Supporting Information).

The bimodal DAB model was fitted to USANS data post galvanostatic cycling, with B fixed to 0.117 cm^{-1} in line with the negligible background, as shown in Figure S11 and Table S5 (Supporting Information), with microstructural parameters and derived surface area shown in **Figures 4** and **5**. The reliability of parameters refined using USANS data is discussed in Note S5, Figures S12–S14, and Table S6 (Supporting Information). L_{nano} was ≈240 and 170 nm for the cell cycled at 2 and 20 mA cm^{-2}, respectively, comparable to the width of lithium "whiskers" observed by electron microscopy,[5b,e,23] and where a reduction of whisker width was observed with increasing current density.[5e,22] The surface area is found exclusively dependent on D_{nano} and L_{nano}, with negligible influence from micrometric lithium. This corresponds to surface area per unit area S_A from 60 to 300 cm^2 cm^{-2} in the 2 mA cm^{-2} cell and ≈ 400 cm^2 cm^{-2} in the 20 mA cm^{-2} cell, within an order of magnitude of those determined by gas adsorption (Table 1). Cycling history of the cell had a major impact on the evolution of surface area, where 1 h at 20 mA cm^{-2} caused a smaller increase in S_V when the cell was previously cycled at 2 mA cm^{-2} compared to 20 mA cm^{-2}, noting that capacity may have been limited by dendrite-induced short circuits. With increasing cycling, parameters for the cell cycled at 2 mA cm^{-2} approached values obtained for the cell cycled at 20 mA cm^{-2}. A fuller description of lithium structural information derived from the bimodal DAB model is given in Note S6 (Supporting Information).

4. Conclusion

In conclusion, we have studied a lithium metal battery (LMB) with relatively simple pouch construction using in situ small angle neutron scattering (SANS) and ultra-small angle neutron scattering (USANS) and demonstrate how these data can be used to derive details of the structural development of deposited lithium within LMBs. We show that structural characteristics of the deposited lithium can be evaluated with good precision and much less difficulty compared to other techniques such as X-ray tomography, microscopy, or gas adsorption. We demonstrate the sensitivity of SANS and USANS to the development of lithium-electrolyte interfaces arising from lithium deposition and quantify the surface area and average distance between these interfaces using relatively simple Porod's law and Debye–Anderson–Brumberger models applied to the SANS and USANS data, respectively. Complex variations of surface area and distance between interfaces were observed depending on the cell cycling history. This work paves the way for future investigations probing the influence of parameters such as current density, charge duration, and alternating lithium deposition/dissolution processes on the surface area and interfacial distances within the deposited lithium, with such information necessary to address the limitations that lithium dendrite growth has on LMB technology application.

5. Experimental Section

Battery Components: Three separators were investigated: polypropylene (Celgard 2400 Polypore, 25 µm thickness, 40 nm pore size, 40% porosity), polyvinylidene difluoride (PVDF) (Immobilon-P, Merck, 110 µm

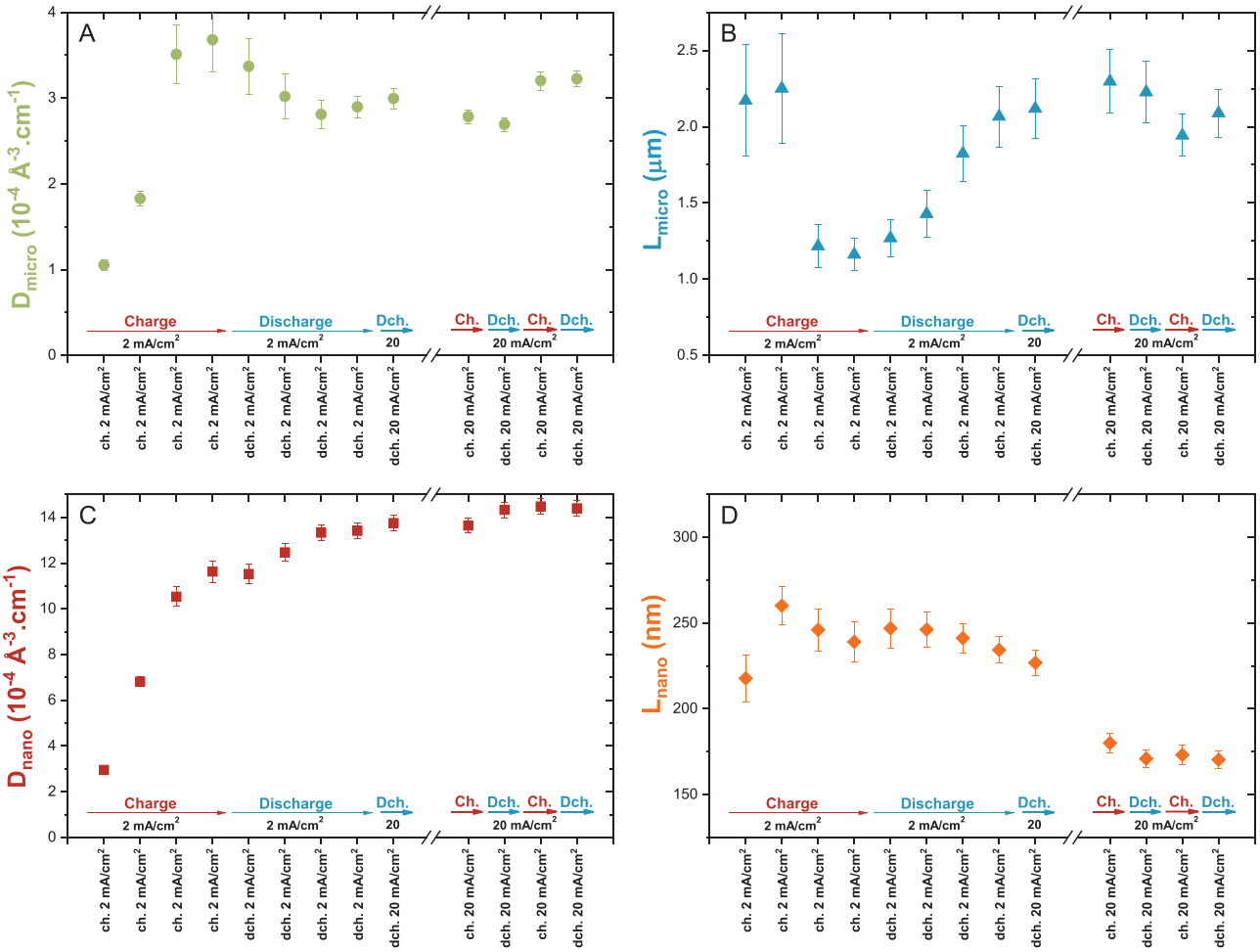

Figure 4. Microstructural parameters of surface lithium extracted from the bimodal DAB model. Refined parameters of the bimodal DAB model for lithium using USANS data of the in situ cell after each galvanostatic step, where "Ch." and "Dch." refer to "charge" and "discharge", respectively. A) Scale factor of micrometric features D_{micro}, B) correlation length L_{micro}, C) Scale factor of nanometric features D_{nano}, and D) correlation length L_{nano}. Error bars are standard uncertainties estimated from least-squares regression.

thickness, 450 nm pore size, 70% porosity), and quartz glass microfibre (Whatman QM/A, Sigma–Aldrich, 450 µm thickness, 2.2 µm pore size). Four current collectors were investigated: nickel mesh (TOB New Energy, 180 µm aperture, 50 µm threads), copper mesh (99.9%, The Mesh Company, 204 µm aperture, 50 µm threads), electrodeposited copper foil with one rough and one smooth side (> 98%, MTI, 9 µm thickness), and roll-annealed copper foil smooth on both sides (99.9%, Goodfellow, 25 µm thickness). Current collectors and separators were dried overnight at 80 °C under vacuum before their introduction into an Ar glove box. The electrolyte was made by dissolving 1 M lithium hexafluorophosphate ($LiPF_6$) (99.99%, Sigma–Aldrich) in a 1:1 volume mixture of ethylene carbonate (EC) (anhydrous, 99%, Sigma–Aldrich) and dimethyl carbonate (DMC) (anhydrous, 99.7%, Sigma–Aldrich). Solvents were dried overnight under 4A molecular sieves prior to dissolution of $LiPF_6$ at room temperature for two days within an Ar-filled glove box with <1 ppm O_2 and H_2O. Lithium metal (99.9%, Goodfellow, 200 µm thickness) was used as electrodes. Although lithium was stored in an Ar-filled glove box with <1 ppm O_2 and H_2O, a thin and uneven coating of a black or white crust as a result of oxidation or nitridation, respectively, was present on the lithium metal, which was removed by abrasion using a rough polypropylene block until a metallic surface of color typical for lithium metal was obtained. Aluminum laminated film (MTI, 115 µm thickness), referred to as laminated pouch, was used for isolating air-sensitive battery components, consisting of an inner polypropylene layer facing battery components and an outer nylon 6,6 polyamide layer, with the two layers encasing a layer of aluminum metal, attached with adhesive of unknown composition (not provided by the manufacturer).

SANS and USANS data from individual battery components were collected to quantify their contribution to the overall scattering signal from the cell and to inform the construction of a symmetrical pouch cell favorable to the observation of changes in the deposited lithium. Laminated Al pouch, separators, and current collectors were handled in air. Lithium metal and separators wetted with ≈ 200 µL electrolyte were sealed in the laminated Al casing within an Ar glove box. Components, aside from the electrolyte, were maintained flat between two quartz plates and taped to a flat sample holder during SANS and USANS measurements (Figure 1D). Electrolyte was introduced between two quartz plates separated by 300 µm and sealed with a compressed O-ring during USANS measurements and introduced into a quartz cuvette (Hellma cell) of 1 mm thickness and sealed by a Teflon cap for SANS measurements. Quartz plate and cuvette scattering measurements were also made and formed part of the empty cell measurements used in the background subtraction during data processing.

Preparation of Symmetrical Cells and Electrochemical Cycling During In Situ SANS and USANS Data Collection: Two symmetrical lithium metal pouch cells were prepared in an Ar-filled glove box with <1 ppm O_2 and

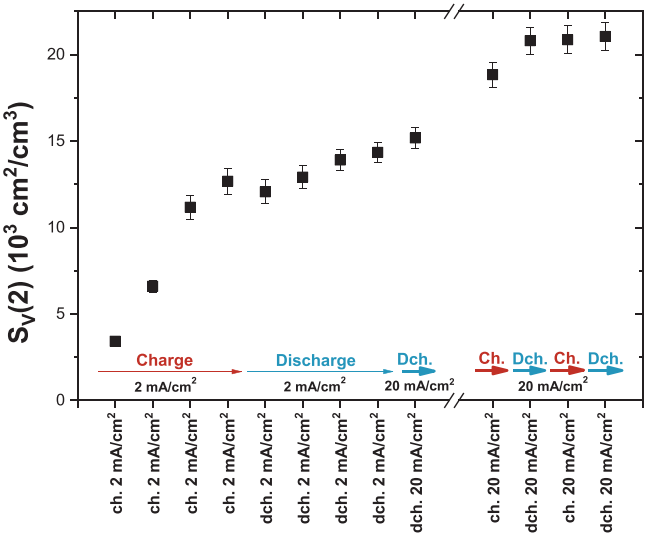

Figure 5. Surface area derived from the bimodal DAB model. Refined surface area per unit volume $S_V(2)$ considering two phases (lithium and the electrolyte) calculated from refined parameters of the bimodal DAB model using USANS data for lithium in the in situ cell after each galvanostatic step. Error bars are standard uncertainties estimated from least-squares regression.

H_2O. Lithium foil electrodes 2.5 cm × 2.5 cm, comprising ≈10 mg cm^{-2} (38.6 mAh cm^{-2}), were placed on 3.0 cm × 4.0 cm roll-annealed copper current collectors and aligned on each side of a PVDF separator wetted with ≈200 µL of 1 M $LiPF_6$ in EC/DMC electrolyte. Measurements of cut lithium square electrodes post abrasion showed a thickness of 200 ± 10 µm, edge length of 2.5 ± 0.1 cm, and initial mass 62 ± 4 mg. The assembly was sealed in a laminated aluminum pouch and electrical connections made with Ni tabs mechanically welded to current collectors. A representation of the cell is shown in Figure 1A–C.

Batteries were maintained flat between quartz plates with a slight pressure applied by bulldog clips to prevent misalignment of electrodes. The two nominally identical symmetrical lithium metal in situ cells each underwent electrochemical cycling at different applied current density, which influences the rate at which lithium was deposited and extracted from electrode surfaces. Although the terms "charge" and "discharge" have no real meaning in a symmetrical cell where lithium is in excess, they were used here to indicate when the direction of applied current is reversed. One cell underwent two cycles (alternating "charge" and "discharge" processes) at 20 mA cm^{-2} and the other cell underwent four consecutive "charges" followed by four consecutive "discharges" at 2 mA cm^{-2}, with a final "discharge" at 20 mA cm^{-2}.

Each galvanostatic step was applied for 1 h using a PG302N (Autolab) potentiostat/galvanostat and the circuit was left open for 3–5 h during which USANS data were measured. SANS data of the 20 mA cm^{-2} battery were measured prior to and following cycling in USANS studies. Applied current and measured voltage are shown in Figure S15 (Supporting Information). The calculated amount of lithium exchanged after each galvanostatic step is 5.2 ± 0.4 and 0.52 ± 0.04 mg cm^{-2} at 20 and 2 mA cm^{-2}, respectively, and the calculated mass of lithium in each electrode is shown in Figure S10 (Supporting Information), assuming this as a total inventory with no loss from side reactions and the complete reinsertion of previously deposited lithium on current reversal. The mass of lithium m_{Li} exchanged between electrodes after a current I was applied for a time t was calculated by $m_{Li} = \frac{Ixt}{F} \times M_{Li}$ where F = 96 485 A.s mol^{-1} is the Faraday constant and M_{Li} = 6.94 g mol^{-1} is the molar mass of lithium. After cycling, both cells showed tighter compression against quartz plates, consistent with lithium volume expansion from increased surface porosity.[24]

Small and Ultra-Small Angle Neutron Scattering Measurements and Calibration: USANS data (approximate Q range = 3.5 × 10^{-5} – 10^{-2} Å^{-1}) were measured on the slit-geometry instrument Kookaburra at the Australian Nuclear Science and Technology Organization (ANSTO)[25] in high flux mode with a neutron wavelength of 4.74 Å and vertical resolution parameter of 0.0586 Å^{-1}. The beam aperture diameter was 29 mm for individual components and 12 mm for cells. Multiple scattering was estimated from USANS data using the beam transmission T_{SAS} method[15,26] using neutron counts measured with and without the sample to estimate neutron transmission through the sample after attenuation by coherent, incoherent scattering, and absorption combined ($T_{A,I,C}$), by absorption and incoherent scattering combined ($T_{A,I}$), and by coherent scattering only (T_{SAS}), the latter with < 70% may be an indication of multiple scattering.

SANS data were measured on the pinhole-geometry instrument Quokka at ANSTO[27] in four configurations: at a neutron wavelength of ≈5.0 Å and sample-to-sample detector distances of 20.1, 8.0, and 1.3 m, and at a wavelength of ≈ 8.1 Å and sample to detector distance of 20.1 m using MgF_2 focusing optics. The minimum available Q was 6 × 10^{-4} Å^{-1} while the upper cut-off was determined to be ≈ 0.1 A^{-1} as a result of attaching the samples to the front face of the automatic sample changer. Quokka features a 1 × 1 m^2 area detector that was used to identify anisotropic scattering from individual cell components.

The experimentally measured scattering intensity was converted to differential macroscopic scattering cross-section per unit volume (absolute calibration) using empty-beam and direct beam attenuation measurements,[28] and taking into account the thickness of components given previously. For each component i, the differential scattering cross-section per unit area I_A (in cm^2.cm^{-2}) and per unit volume I_V (in cm^{-1}) are related by the thickness t (in cm) of the component:

$$I_A\ (i) = I_V\ (i) \times t\ (i) \tag{7}$$

When a sample contains several components i (sample = $\sum i$) and component scattering is independent - as demonstrated for those comprising the in situ cell except for separator and electrolyte treated together - scattering intensities per unit area are additive:

$$I_A\left(\sum i\right) = \sum_i I_A\ (i) \tag{8}$$

and scattering per unit volume is obtained after multiplication by the thickness:

$$I_V\left(\sum i\right) \times \sum_i t\ (i) = \sum_i \left[I_V\ (i) \times t\ (i)\right] \tag{9}$$

For example, the differential scattering cross-section per unit volume for the in situ cell corresponds to the sum of scattering of each component multiplied by their thickness:

$$\mathrm{I_V\ (cell)} \times [t\ (\mathrm{Li}) + t\ (\mathrm{Cu}) + t\ (\mathrm{PVDF}) + t\ (\mathrm{pouch})] = \tag{10}$$

$$\mathrm{I_V\ (Li)} \times t\ (\mathrm{Li}) + I_V\ (\mathrm{Cu}) \times t\ (\mathrm{Cu}) + I_V\ (\mathrm{PVDF})$$

$$\times t\ (\mathrm{PVDF}) + \mathrm{I_V\ (pouch)} \times t\ (\mathrm{pouch})$$

where Li, Cu, PVDF and pouch denote lithium foils, smooth copper foils, electrolyte-wet PVDF and the laminated pouch. The scattering per unit volume for lithium in the in situ cell is:

$$I_V\ (\mathrm{Li}) = \begin{bmatrix} I_V\ (\mathrm{cell}) \times [t\ (\mathrm{Li}) + t\ (\mathrm{Cu}) + t\ (\mathrm{PVDF}) + t\ (\mathrm{pouch})] \\ -I_V\ (\mathrm{Cu}) \times t\ (\mathrm{Cu}) - I_V\ (\mathrm{PVDF}) \times t\ (\mathrm{PVDF}) - I_V\ (\mathrm{pouch}) \times t\ (\mathrm{pouch}) \end{bmatrix} \div t\ (Li) \tag{11}$$

using thicknesses as given previously, with t(Li) = 2 × 200 µm, t(Cu) = 2 × 25 µm, t(PVDF) = 110 µm and t(pouch) = 2× 115 µm. Scattering data for lithium within in situ cells are shown as a differential cross-section per unit volume and considers the constant initial volume of lithium in the cell (2 × 200 µm × beam area) ignoring volume changes.

Data were subsequently processed using Python manipulations in Mantid[29] for additions, subtractions, and, in the case of USANS data, desmearing. Data additions and subtractions were performed independently for SANS and slit-smeared USANS after a spline interpolation of the data to a common Q grid of evenly spaced points on a log-scale. For plotting purposes, USANS data were desmeared as the last step using the Lake algorithm.[30] Differential scattering cross-sections are given with solid angles expressed in units of steradians but steradians were omitted from unit labels by convention.[31] In plot axis labels, "differential scattering cross-section" is simplified to "scattering intensity". Model fitting was done using the program SASView 5.0.5 for slit-smeared USANS and/or SANS data, with horizontal slit-smearing applied to the model when USANS data were included. Standard uncertainties of refined parameters are estimated from least-squares regression following recommendations of the International Union of Crystallography.[32]

Surface Area Conversions: For calculations of surface areas, the coherent neutron scattering length density (SLD) was calculated using $SLD = \frac{N_A \rho}{M} \times \sum_i p_i b_{C,i}$ where N_A is Avogadro's number, ρ is the bulk density, M is the molar mass, $b_{C,i}$ are the atomic coherent scattering lengths[33] of the i element in atomic proportion p_i.

The surface area per unit volume S_V (cm^2 cm^{-3}) extracted from the coherent scattering cross-section per lithium volume corresponds to the surface contributing to scattering S_i divided by the initial volume of lithium introduced in the cell:

$$S_V = \frac{S_i}{\text{initial Li volume}} = \frac{S_i}{\text{beam area} \times \text{foil thickness} \times \text{number of foils}} \quad (12)$$

with two 200 µm-thick lithium foils in our experiment, neglecting thickness changes after cycling. The surface area per unit mass S_M (cm^2 g^{-1}) is derived from S_V:

$$S_M = \frac{S_i}{\text{initial Li mass}} = \frac{S_i}{\text{beam area} \times \text{mass loading} \times \text{number of foils}} = \frac{S_V \times \text{foil thickness}}{\text{mass loading}} \quad (13)$$

with a mass loading of ≈9.9 ± 1.4 mg cm^{-2} in the experiment. Both S_V and S_M average the surface of the lithium–electrolyte interface over the total lithium inventory, including excess lithium, precluding comparison between cells with different amounts of lithium. Since surface scattering scales with sample area rather than volume,[34] the surface area per unit area S_A (cm^2 cm^{-2}), where only active lithium surfaces are considered, can be derived from S_V, considering one active electrode surface on each foil:

$$S_A = \frac{S_i}{\text{active Li surface in the beam}} = \frac{S_i}{\text{beam area} \times \text{number of foils}} = S_V \times \text{foil thickness} \quad (14)$$

Supporting Information

Supporting Information is available from the Wiley Online Library or from the author.

Acknowledgements

Access to Kookaburra and Quokka instruments was supported by ANSTO beamtime awards (proposal P8690 and DB9219). This work benefited from the use of the SasView program, originally developed under NSF award DMR-0520547. SasView contains code developed with funding from the European Union's Horizon 2020 research and innovation programme under the SINE2020 project, grant agreement No 654000. Authors are grateful to Liliana de Campo for troubleshooting issues with using the SasView program and useful discussions.

Open access publishing facilitated by Australian Nuclear Science and Technology Organisation, as part of the Wiley - Australian Nuclear Science and Technology Organisation agreement via the Council of Australian University Librarians.

Conflict of Interest

The authors declare no conflict of interest.

Data Availability Statement

The data that support the findings of this study are available from the corresponding author upon reasonable request.

Keywords

batteries, dendrites, lithium metal, small angle neutron scattering

Received: April 27, 2023
Revised: August 31, 2023
Published online:

[1] G. E. Blomgren, *J. Electrochem. Soc.* **2017**, *164*, A5019.
[2] a) D. Aurbach, E. Zinigrad, H. Teller, P. Dan, *J. Electrochem. Soc.* **2000**, *147*, 1274; b) D. Lin, Y. Liu, Y. Cui, *Nat. Nanotechnol.* **2017**, *12*, 194.
[3] a) J. I. Yamaki, S. I. Tobishima, K. Hayashi, Keiichi Saito, Y. Nemoto, M. Arakawa, *J. Power Sources* **1998**, *74*, 219; b) W. Xu, J. Wang, F. Ding, X. Chen, E. Nasybulin, Y. Zhang, J.-G. Zhang, *Energy Environ Sci* **2014**, *7*, 513.
[4] a) L. Frenck, G. K. Sethi, J. A. Maslyn, N. P. Balsara, *Front. Energy Res.* **2019**, *7*, 115; b) J. L. Ma, F.-L. Meng, Y. Yu, D.-P. Liu, J. M. Yan, Y. Zhang, X.-B. Zhang, Q. Jiang, *Nat. Chem.* **2019**, *11*, 64; c) Y. Yin, Y. Yang, D. Cheng, M. Mayer, J. Holoubek, W. Li, G. Raghavendran, A. Liu, B. Lu, D. M. Davies, Z. Chen, O. Borodin, Y. S. Meng, *Nat. Energy* **2022**, *7*, 548; d) C. Fang, B. Lu, G. Pawar, M. Zhang, D. Cheng, S. Chen, M. Ceja, J. M. Doux, H. Musrock, M. Cai, B. Liaw, Y. S. Meng, *Nat. Energy* **2021**, *6*, 987; e) J. Wang, W. Huang, A. Pei, Y. Li, F. Shi, X. Yu, Y. Cui, *Nat. Energy* **2019**, *4*, 664.
[5] a) P. Bai, J. Li, F. R. Brushett, M. Z. Bazant, *Energy Environ. Sci.* **2016**, *9*, 3221; b) A. Kushima, K. P. So, C. Su, P. Bai, N. Kuriyama, T. Maebashi, Y. Fujiwara, M. Z. Bazant, J. Li, *Nano Energy* **2017**, *32*, 271; c) J. Steiger, D. Kramer, R. Mönig, *Electrochim. Acta* **2014**, *136*, 529; d) H. Kühnle, E. Knobbe, E. Figgemeier, *J. Electrochem. Soc.* **2022**, *169*, 040528; e) Y. Xu, H. Wu, H. Jia, J.-G. Zhang, W. Xu, C. Wang, *ACS Nano* **2020**, *14*, 8766.
[6] P. Bai, J. Guo, M. Wang, A. Kushima, L. Su, J. Li, F. R. Brushett, M. Z. Bazant, *Joule* **2018**, *2*, 2434.
[7] a) O. O. Taiwo, D. P. Finegan, J. M. Paz-Garcia, D. S. Eastwood, A. J. Bodey, C. Rau, S. A. Hall, D. J. L. Brett, P. D. Lee, P. R. Shearing, *Phys. Chem. Chem. Phys.* **2017**, *19*, 22111; b) J.-H. Cheng, A. A. Assegie, C. J. Huang, M. H. Lin, A. M. Tripathi, C. C. Wang, M. T. Tang, Y. F. Song, W. N. Su, B. J. Hwang, *J. Phys. Chem. C* **2017**, *121*, 7761.
[8] S. Basak, K. Dzieciol, Y. E. Durmus, H. Tempel, H. Kungl, C. George, J. Mayer, R. A. Eichel, *Chem. Phys. Rev.* **2022**, *3*, 031303.
[9] R. Bhattacharyya, B. Key, H. Chen, A. S. Best, A. F. Hollenkamp, C. P. Grey, *Nat. Mater.* **2010**, *9*, 504.

[10] S. Risse, E. Härk, B. Kent, M. Ballauff, *ACS Nano* **2019**, *13*, 10233.
[11] R. L. Sacci, J. L. Bañuelos, G. M. Veith, K. C. Littrell, Y. Q. Cheng, C. U. Wildgruber, L. L. Jones, A. J. Ramirez-Cuesta, G. Rother, N. J. Dudney, *J. Phys. Chem. C* **2015**, *119*, 9816.
[12] C. J. Jafta, C. A. Bridges, Y. Bai, L. Geng, B. P. Thapaliya, H. M. Meyer, R. Essehli, W. T. Heller, I. Belharouak, *ChemSusChem* **2020**, *13*, 3654.
[13] a) S. Seidlmayer, J. Hattendorff, I. Buchberger, L. Karge, H. A. Gasteiger, R. Gilles, *J. Electrochem. Soc.* **2015**, *162*, A3116; b) J. Hattendorff, S. Seidlmayer, H. A. Gasteiger, R. Gilles, *J. Appl. Crystallogr.* **2020**, *53*, 210.
[14] J. Yang, F. Mo, J. Hu, S. Li, L. Huang, F. Fang, D. Sun, G. Sun, F. Wang, Y. Song, *Appl. Phys. Lett.* **2022**, *121*, 163901.
[15] Y. Ji, A. P. Radlinski, T. Blach, L. De Campo, P. Vu, H. Roshan, K. Regenauer-Lieb, *Fuel* **2022**, *325*, 124957.
[16] a) K. Saito, M. Arakawa, S. Tobishima, J. Yamaki, *J. Power Sources* **1998**, *72*, 111; b) R. Weber, J.-H. Cheng, A. J. Louli, M. Coon, S. Hy, J. R. Dahn, *J. Electrochem. Soc.* **2019**, *166*, A3250.
[17] a) G. Porod, in *Small-Angle X-Ray Scattering*, (Eds: O. Glatter, O. Kratky), London **1982**, 2; b) O. Glatter, O. Kratky, *Small-Angle X-Ray Scattering*, Academic, London **1982**.
[18] a) H. Pan, T. Fu, G. Zan, R. Chen, C. Yao, Q. Li, P. Pianetta, K. Zhang, Y. Liu, X. Yu, H. Li, *Nano Lett.* **2021**, *21*, 5254; b) M. Sadd, S. Xiong, J. R. Bowen, F. Marone, A. Matic, *Nat. Commun.* **2023**, *14*, 854.
[19] a) P. Debye, H. R. Anderson, H. Brumberger, *J. Appl. Phys.* **1957**, 28; b) P. Debye, A. M. Bueche, *J. Appl. Phys.* **1949**, *20*, 518.
[20] a) H. Liu, X. B. Cheng, R. Xu, X. Q. Zhang, C. Yan, J.-Q. Huang, Q. Zhang, *Adv. Energy Mater.* **2019**, *9*, 1902254; b) K. N. Wood, E. Kazyak, A. F. Chadwick, K. H. Chen, J.-G. Zhang, K. Thornton, N. P. Dasgupta, *ACS Cent. Sci.* **2016**, *2*, 790; c) L. Gireaud, S. Grugeon, S. Laruelle, B. Yrieix, J. M. Tarascon, *Electrochem. Commun.* **2006**, *8*, 1639.
[21] M. Born, E. Wolf, A. Bhatia, P. Clemmow, D. Gabor, A. Stokes, A. M. Taylor, P. A. Wayman, W. Wilcock, *Principles of optics: electromagnetic theory of propagation, interference and diffraction of light*, 7th ed., Cambridge University Press, Cambridge **1999**.
[22] K. Dong, Y. Xu, J. Tan, M. Osenberg, F. Sun, Z. Kochovski, D. T. Pham, S. Mei, A. Hilger, E. Ryan, Y. Lu, J. Banhart, I. Manke, *ACS Energy Lett.* **2021**, *6*, 1719.
[23] Y. Li, Y. Li, A. Pei, K. Yan, Y. Sun, C. L. Wu, L. M. Joubert, R. Chin, A. L. Koh, Y. Yu, J. Perrino, B. Butz, S. Chu, Y. Cui, *Science* **2017**, *358*, 506.
[24] K. Ariyoshi, Y. Yamamoto, *J. Power Sources* **2022**, *533*, 231360.
[25] C. Rehm, L. De Campo, A. Brûlé, F. Darmann, F. Bartsch, A. Berry, *J. Appl. Crystallogr.* **2018**, *51*, 1.
[26] G. V. Jensen, J. G. Barker, *J. Appl. Crystallogr.* **2018**, *51*, 1455.
[27] K. Wood, J. P. Mata, C. J. Garvey, C. M. Wu, W. A. Hamilton, P. Abbeywick, D. Bartlett, F. Bartsch, P. Baxter, N. Booth, W. Brown, J. Christoforidis, D. Clowes, T. D'adam, F. Darmann, M. Deura, S. Harrison, N. Hauser, G. Horton, D. Federici, F. Franceschini, P. Hanson, E. Imamovic, P. Imperia, M. Jones, S. Kennedy, S. Kim, T. Lam, W. T. Lee, M. Lesha, et al., *J. Appl. Crystallogr.* **2018**, *51*, 294.
[28] a) G. D. Wignall, F. S. Bates, *J. Appl. Crystallogr.* **1987**, *20*, 28; b) S. R. Kline, *J. Appl. Crystallogr.* **2006**, *39*, 895.
[29] O. Arnold, J. C. Bilheux, J. M. Borreguero, A. Buts, S. I. Campbell, L. Chapon, M. Doucet, N. Draper, R. Ferraz Leal, M. A. Gigg, V. E. Lynch, A. Markvardsen, D. J. Mikkelson, R. L. Mikkelson, R. Miller, K. Palmen, P. Parker, G. Passos, T. G. Perring, P. F. Peterson, S. Ren, M. A. Reuter, A. T. Savici, R. J. Taylor, R. Tolchenov, W. Zhou, J. Zikovsky, *Nucl. Instrum. Methods Phys. Res., Sect. A* **2014**, *764*, 156.
[30] J. A. Lake, *Acta Crystallogr.* **1967**, *23*, 191.
[31] BIPM, *Bureau international des poids et mesures*, 9th ed., Online **2019**.
[32] D. Schwarzenbach, S. C. Abrahams, H. D. Flack, E. Prince, A. J. C. Wilson, *Acta Crystallogr.* **1995**, *A51*, 565.
[33] V. F. Sears, *J. Neutron Res.* **1992**, *3*, 26.
[34] M. Roth, *J. Appl. Crystallogr.* **1977**, *10*, 172.